



Mirror Mode Waves Immersed in Magnetic Reconnection

L.-N. Hau^{1,2} , G.-W. Chen¹ , and C.-K. Chang¹ ¹ Department of Space Science and Engineering, National Central University, Taoyuan City, Taiwan R.O.C.² Department of Physics, National Central University, Taoyuan City, Taiwan R.O.C.

Received 2020 September 4; revised 2020 October 2; accepted 2020 October 2; published 2020 October 29

Abstract

Mirror mode waves with anticorrelated density and magnetic field are widely observed in the heliosphere. This paper presents the first evidence of mirror mode waves occurring in the vicinity of a magnetic reconnection site (X-line) at the interface between the solar wind and Earth's magnetosphere based on the analyses of two Magnetospheric Multiscale (MMS) crossing events along with the Grad-Shafranov (GS) reconstruction model with temperature anisotropy. The GS scheme solves the steady two-dimensional MHD equations in the frame of references moving with the plasma by using the spacecraft measurements. Both events have mirror type of pressure anisotropy and correspond, respectively, to the symmetric and asymmetric Harris type current sheets with the total thermal and magnetic field pressures being approximately constant. The GS reconstruction results show the magnetic reconnection with X line geometry associated with the mirror mode structures on the spatial lengths of 170 ~ 370 km or 1.3 ~ 3 ion gyroradius. The coexistence of mirror waves and magnetic reconnection provides the first observational evidence for the prior theoretical prediction of mixed tearing and mirror instabilities in plasma current sheets with temperature anisotropy.

Unified Astronomy Thesaurus concepts: [Magnetohydrodynamics \(1964\)](#); [Space plasmas \(1544\)](#); [Plasma astrophysics \(1261\)](#); [Plasma physics \(2089\)](#); [Alfvén waves \(23\)](#)

1. Introduction

In space and astrophysical plasma environments temperature anisotropy may easily develop due to the lack of sufficient collisions. For $T_{\perp}/T_{\parallel} > (1 + \beta_{\perp})/\beta_{\perp}$, the mirror instability may arise (Hasegawa 1969), where $\beta = P/(B^2/2\mu_0)$ and the subscripts denote the components parallel and perpendicular to the magnetic field. The mirror mode waves characterized by the anticorrelated density and magnetic field have been widely observed in the solar wind, planetary magnetospheres, heliosheath, etc. (Joy et al. 2006; Burlaga et al. 2007; Tsurutani et al. 2011). The mirror structures observed in the magnetosheath are typically of 10–40 ion inertial lengths (Horbury & Lucek 2009; Hau et al. 2020). Kinetic mirror structures with a few proton or electron gyroradii have also been identified in the magnetosphere, solar wind, and foreshock (Gershman et al. 2016; Liu et al. 2019; Yao et al. 2019). Theoretical efforts have focused mostly on the kinetic aspects of mirror instability including the stability criteria, growth rates, etc. (Ferrière & André 2002). Recently there have been a few studies examining the two-dimensional (2D) structures of observed mirror waves based on the Grad-Shafranov reconstruction (GSR) technique (Teh 2019; Hau et al. 2020; Tian et al. 2020). The GSR models solve the steady 2D MHD equilibrium in the comoving frame of reference from the plasma and magnetic field measurements by a single spacecraft (Hau & Sonnerup 1999; Sonnerup et al. 2006). In the so-called deHoffmann-Teller (HT) frame the convective electric field $\mathbf{E} = -\mathbf{V} \times \mathbf{B}$ nearly vanishes (Sonnerup et al. 1987) so that the coherent structures may be modeled by the field-aligned MHD theory (Sonnerup et al. 1992). The viability of applying the GSR methods with temperature anisotropy to the mirror waves was recently demonstrated by comparing the MHD

or Hall MHD simulations with reconstruction results (Hau et al. 2020).

Magnetic reconnection (MR) may occur in various space and astrophysical plasma environments, among which the planetary magnetopause boundaries separating the solar wind and magnetospheric origins of plasmas and magnetic field are some of the most likely sites for the occurrence of MR. Due to the easy access to the in situ spacecraft observations the Earth's magnetopause is the most widely studied space plasma environment for MR (Paschmann et al. 1979; Vaivads et al. 2004; Graham et al. 2014). In particular, the Magnetospheric Multiscale (MMS) mission has contributed greatly to the kinetic physics of magnetopause reconnection (Burch et al. 2016; Hasegawa et al. 2017; Zhong et al. 2020). Many studies have shown that an initial Harris type equilibrium profile with constant total pressures $P_T = P_{\perp} + B^2/2\mu_0$ and antiparallel magnetic field with or without a guide field (Harris 1962) may tend to develop MR geometry. In particular, two major categories of MR have been proposed: the steady state model with a single X line and the outflow approaching the Alfvén speed (Petschek 1964), and the tearing mode instability with a series of X and O lines and mild plasma velocity (Furth et al. 1963). Numerous fluid and kinetic simulations have been carried out to examine the various aspects of MR processes for the past 50 yr (Hau & Chiou 2001; Guo et al. 2015; Landi et al. 2015). In particular, the effects of pressure or temperature anisotropy on MR have been examined by a number of authors (Chen & Palmadesso 1984; Shi et al. 1987; Birn & Hesse 2001; Chiou & Hau 2002, 2003; Hung et al. 2011). In the MHD models the double-polytropic (DP) laws are widely adopted as the energy closures to study the effects of temperature anisotropy and energy closures on MR and tearing mode instability (Chiou & Hau 2002, 2003; Hung et al. 2011). It is shown that the mirror type temperature anisotropy of $T_{\perp} > T_{\parallel}$ may greatly enhance the growth rate of tearing mode instability and the merging rate of single X-line reconnection. In particular, the coupling of tearing and mirror instabilities may lead to relatively larger magnetic islands as compared to the cases with isotropic pressure and the



Original content from this work may be used under the terms of the [Creative Commons Attribution 4.0 licence](#). Any further distribution of this work must maintain attribution to the author(s) and the title of the work, journal citation and DOI.

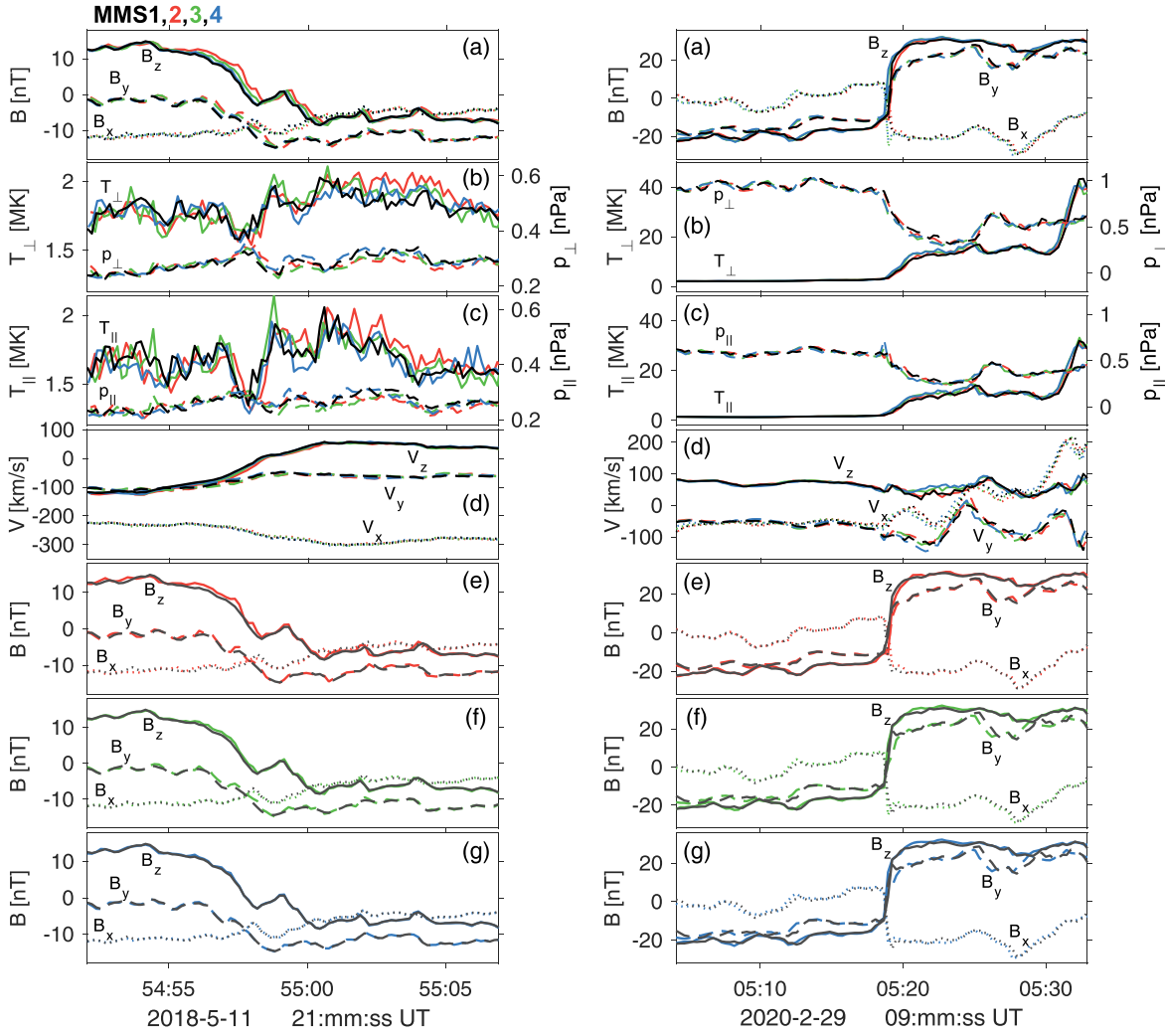


Figure 1. Time series of magnetic field, ion temperatures, thermal pressures, and flow velocity in GSE coordinates for MMS20180511 (left panels) and MMS20200229 (right panels) magnetopause crossing events. The last three panels are the comparisons between MMS observations (colored curves) and GSR predictions (gray curves) at MMS2 (panel (e)), MMS3 (panel (f)), and MMS4 (panel (g)).

mirror waves with anticorrelated density and magnetic field may be present in the vicinity of X lines.

The GSR methods have been widely adopted to reveal the 2D MR occurring in the solar wind, magnetopause, etc., from the spacecraft observations (Hau & Sonnerup 1999; Hu et al. 2003; Hasegawa et al. 2004; Chou & Hau 2012). It is shown that the magnetopause currents often exhibit a single X line or a series of magnetic islands separated by the X lines (Hau & Sonnerup 1999; Chou & Hau 2012). Recently the effects of temperature anisotropy on GSR results are examined for a THEMIS (The Time History of Events and Macroscale Interactions during Substorms) magnetopause crossing (Chen & Hau 2018). It is shown that the mirror type temperature anisotropy of $T_{\perp} > T_{\parallel}$ may yield relatively larger magnetic islands as compared to the isotropic case, which is consistent with the abovementioned theoretical prediction (Chiou & Hau 2002, 2003). This study presents the first evidence of mirror waves adjacent to the X lines by analyzing two MMS magnetopause crossing events along with the anisotropic GSR model. The mirror waves immersed in MR are consistent with the theoretical prediction of the mixed tearing and mirror instabilities in plasma current sheets with temperature anisotropy (Shi et al. 1987; Chiou & Hau 2002, 2003).

2. MMS Magnetopause Crossing Events

We have identified two magnetopause crossing events with the presence of mirror waves in the magnetosheath and magnetosphere observed by the MMS spacecraft. The field and particle data are provided by the fluxgate magnetometer (Russell et al. 2016) and the fast plasma instrument (Pollock et al. 2016). Figure 1 shows the time series of magnetic field, ion thermal pressures, temperatures, and flow velocities in the GSE coordinates for an outbound MMS20180511 crossing (Case A; left panel) and an inbound crossing MMS20200229 (Case B; right panel). Both events have the time resolution of 0.15 seconds. Case A occurring at the nightside dawn flank ($-11.0, -20.3, 7.3$) R_E spans the time interval of 14.85 s (21:54:52.03–21:55:06.88 UT) while Case B occurring at the dayside dawn magnetopause (5.2, $-7.8, 5.8$) R_E spans the time intervals of 28.95 s (09:05:04.05–09:05:33.00 UT). Both events have $T_{\perp} > T_{\parallel}$ ($P_{\perp} > P_{\parallel}$) and all four MMS spacecraft encounter the magnetopause boundary as marked by a reversal in the north-south component of the magnetic field. The magnetic minimum variance analyses (MVA) based on $\nabla \cdot \mathbf{B} = 0$ are used to construct the MVA coordinates (N, M, L) with N being along the magnetopause normal. The convection velocity is inferred from the HT frame analyses based on $\nabla \times (\mathbf{V} \times \mathbf{B}) = 0$. Both cases have high quality of MVA and HT frame analysis results, which

Table 1
Summary of MMS Event Analysis Results

	Case A (20180511)			Case B (20200229)		
MVA eigenvalue	0.38	3.83	101.28	2.87	25.50	958.49
\hat{N}	(-0.72, 0.48, -0.49)			(0.19, -0.74, 0.95)		
\hat{M}	(0.65, 0.74, -0.20)			(0.93, 0.35, 0.11)		
\hat{L}	(-0.26, 0.46, 0.85)			(-0.31, 0.58, 0.75)		
GSR coordinates \hat{x}'	(0.63, -0.135, 0.77)			(0.02, 0.46, -0.89)		
GSR coordinates \hat{y}'	(0.33, -0.85, -0.42)			(-0.49, 0.78, 0.39)		
GSR coordinates \hat{z}'	(0.69, 0.48, -0.55)			(0.87, 0.43, 0.24)		
V_{HT} (km s ⁻¹)	(-320.75, -123.01, 4.17)			(0.05, -44.72, 87.71)		
HT frame correlation coefficient	0.99			0.74		
Walén slope	-1.1			-0.45		
Average λ_i (r_{ci}) in magnetosheath	66.4 km (151.1 km)			42.4 km (99.3 km)		
Average λ_i (r_{ci}) in magnetosphere	70.0 km (127.9 km)			153.4 km (139.9 km)		
Average width of mirror waves in magnetosheath	370.0 km			297.9 km		
Average width of mirror waves in magnetosphere	170.4 km			242.5 km		

show that Case A is a rotational discontinuity-like structure with large field-aligned flow ($V \sim V_A$) and Case B is a tangential discontinuity-like structure with small residual flow ($V \sim 0.2V_A$; $V_A = B/\sqrt{\mu_0\rho}$). The magnetopause normal is $\hat{N} = (-0.72, 0.48, -0.49)$ and the HT velocity is $V_{HT} = (-320.75, -123.01, 4.17)$ km s⁻¹ for Case A, and $\hat{N} = (0.19, -0.74, 0.95)$ and $V_{HT} = (0.05, -44.72, 87.71)$ km s⁻¹ for Case B. Table 1 summarizes the analysis results for MVA, HT frame, Walén relation, characteristic lengths, etc. In particular, the average ion inertial length $\lambda_i = m_i V_A / eB$ and ion gyroradius $r_{ci} = m_i v_{i\perp} / eB$ ($v_{i\perp} = (2k_B T_{\perp} / m_i)^{1/2}$) are $\lambda_i = 66.4$ km and $r_{ci} = 151.1$ km in the magnetosheath, and $\lambda_i = 70$ km and $r_{ci} = 127.9$ km in the magnetosphere for Case A. The average characteristic lengths are $\lambda_i = 42.4$ km and $r_{ci} = 99.3$ km in the magnetosheath, and $\lambda_i = 153.4$ km and $r_{ci} = 139.9$ km in the magnetosphere for Case B.

Figure 2 shows the corresponding density, magnetic field, flow velocity, current density, etc., in the HT frame and MVA coordinates (N, M, L) from the MMS1 spacecraft. In the top panels for the density and magnetic field data, the features of mirror waves with interlacing increased (decreased) density and decreased (increased) magnetic field are clearly seen in Case A but less pronounced in Case B. The bottom two panels show separate plots for the magnetosheath and magnetosphere, indicating pronounced anticorrelated density-magnetic field relationships on both sides of the magnetopause for both cases. For Case A (left panels) the thermal and magnetic field pressures (panel (e)) are more or less the same on both side of the magnetopause with the total pressure $P_T = P_{\perp} + B^2/2\mu_0$ being nearly constant for all of the data intervals (panel (e)). At the magnetopause there is an enhancement in the perpendicular pressure associated with a decrease in the magnetic pressure. The tangential magnetic field profile (panel (b)) shows an antisymmetry and the tangential velocity (panel (c)) also reverses across the current sheet. The overall profiles fit the Harris sheet equilibrium with a guide magnetic field and the mirror waves appear to be superimposed on the average background equilibrium. While for Case B (right panels) the density, thermal pressure, and magnetic field are highly asymmetric. In particular, the density and thermal pressure are relatively larger in the magnetosheath while the magnetic field is relatively larger in the magnetosphere. The total pressures P_T (panel (e)) are more or

less constant except for the central magnetopause region and the overall profiles fit the asymmetric Harris sheet equilibrium.

Also shown in panel (d) of Figure 2 are the plasma β and the mirror parameter $m = \beta_{\perp}/\beta_{\parallel} - (1 + 1/\beta_{\perp})$ normalized by $\beta_{\perp}/\beta_{\parallel} + (1 + 1/\beta_{\perp})$ which measures the degree of mirror instability with $m > 0$ ($m < 0$) being unstable (stable). In Case A, m is close to 0 for all of the intervals while in Case B, m is highly asymmetric with $m > 0$ in the magnetosheath and $m < 0$ in the magnetosphere, respectively. Taking advantage of the multiple spacecraft observations we have calculated the current density for the MMS1 spacecraft based on the four MMS magnetic field data. In particular, the Ampere's law, $\nabla \times \mathbf{B} = \mu_0 \mathbf{J}$, is solved for a tetrahedron geometry (Dunlop et al. 1988), which requires the locations of four spacecraft throughout the data intervals. As indicated in panel (f) of Figure 2, there is relatively larger current density in the transition region between the solar wind and magnetosphere. Note that the magnetopause current density for Case B is 10 times larger than the value of Case A, which is attributed to not only the asymmetric and symmetric profiles of the thermal pressures and magnetic field strength but also the relatively thinner and thicker current layers at the dayside (Case B) and flank (Case A) magnetopause, respectively (Haaland et al. 2020).

3. Grad-Shafranov Reconstruction

The model equations consist of steady ideal 2D MHD equations with field-aligned flow and anisotropic pressures described by the double-polytropic (DP) energy closures of $d(p_{\perp}/\rho B^{\gamma_{\perp}-1})/dt = 0$ and $d(p_{\parallel} B^{\gamma_{\parallel}-1}/\rho^{\gamma_{\parallel}})/dt = 0$, which may incorporate various thermodynamic conditions including the double-adiabatic ($\gamma_{\perp} = 2$ and $\gamma_{\parallel} = 3$) and double-isothermal ($\gamma_{\perp} = 1$ and $\gamma_{\parallel} = 1$) limits. For $\gamma_{\perp} = 2$ and $\gamma_{\parallel} = 0.5$, the mirror instability criteria derived based on the DP MHD model are consistent with the kinetic results (Hau & Sonnerup 1993). The DP GS equation has the following form.

$$\nabla \cdot [(1 - M_A^2)(1 - \alpha)\nabla A] = \mu_0 \rho \left[T_{\perp} \left(\frac{dS_{\perp}}{dA} \right) + T_{\parallel} \left(\frac{dS_{\parallel}}{dA} \right) - \left(\frac{dH}{dA} \right) \right] - B_z \left(\frac{dC_z}{dA} \right) - \frac{B^2}{2\mu_0 \rho} \left(\frac{dG^2}{dA} \right), \quad (1)$$

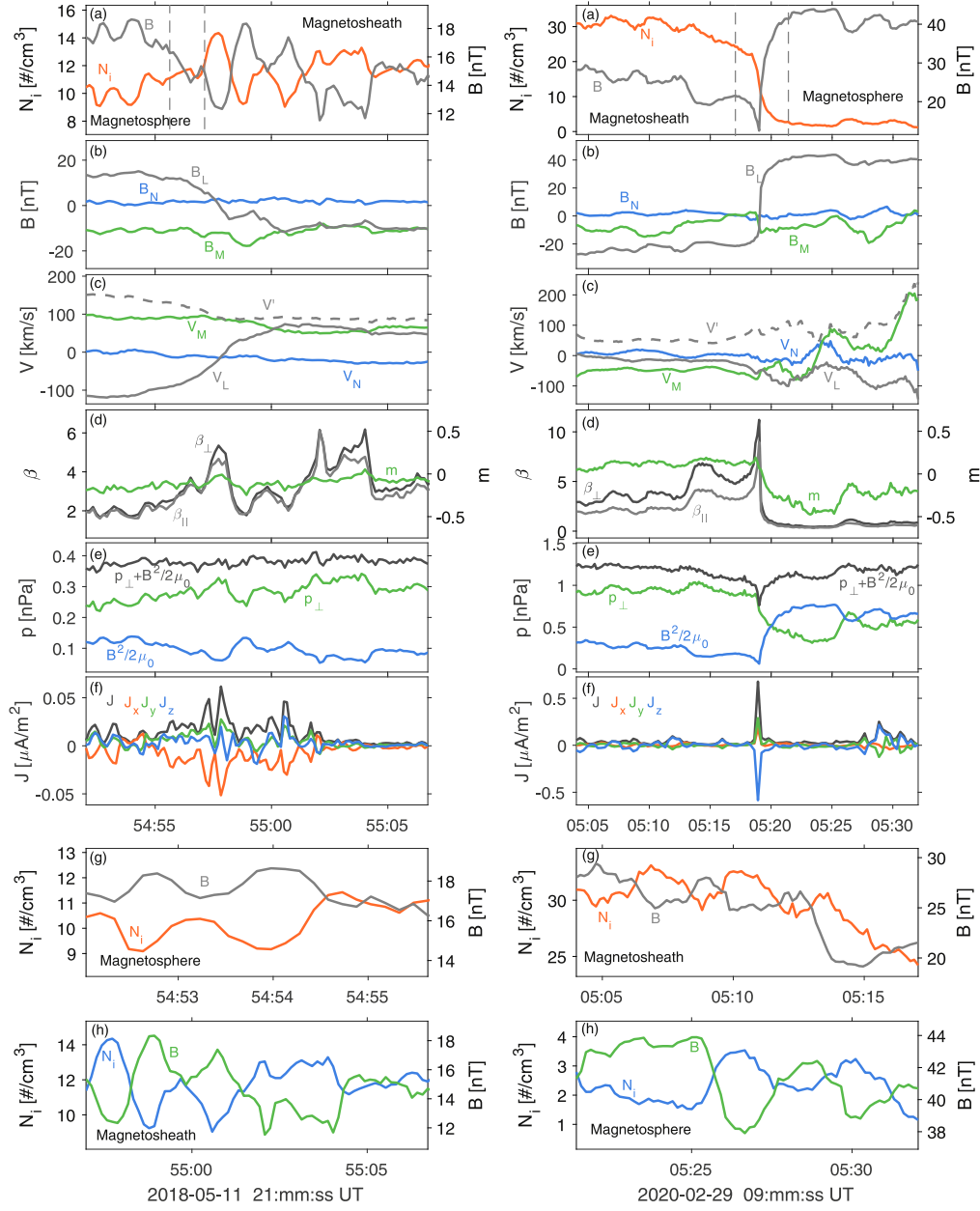


Figure 2. Time series of MMS20180511 (left panels) and MMS20200229 (right panels) data in *NML* coordinates and HT frame. The parameter m in panel (d) measures the mirror instability and panel (f) is the current density in GSR coordinates with \hat{z}' being along the invariant axis. The bottom two panels are the ion density and magnetic field for the magnetosheath and magnetospheric sides of the data intervals marked in panel (a).

in which A is the magnetic vector potential, $\alpha = \mu_0(P_{\parallel} - P_{\perp})/B^2$, and $M_A = V/V_A = V/(B\sqrt{(1-\alpha)/\mu_0\rho})$ with the five field-aligned invariants, $S_{\perp} = c_{v\perp} \ln(P_{\perp}/\rho B^{\gamma_{\perp}-1})$, $S_{\parallel} = c_{v\parallel} \ln(P_{\parallel} B^{\gamma_{\parallel}-1}/\rho^{\gamma_{\parallel}})$, $G = M_A \sqrt{\mu_0\rho(1-\alpha)}$, $C_z = (1-\alpha)(1-M_A^2)B_z$, and $H = (\gamma_{\perp}-1)^{-1}P_{\perp}/\rho + \gamma_{\parallel}(\gamma_{\parallel}-1)^{-1}P_{\parallel}/\rho + V^2/2$ ($H = (p_{\perp}/\rho) \log B + (p_{\parallel}/\rho) \log(\rho/B) + V^2/2$ for $\gamma_{\perp} = \gamma_{\parallel} = 1$). Equation (1) needs be completed by the following auxiliary relations:

$$\mathcal{M}\mathcal{X}^T = \mathcal{Y}^T \quad (2)$$

$$\mathcal{X} = \left[\frac{\partial p_{\perp}}{\partial y}, \frac{\partial p_{\parallel}}{\partial y}, \frac{\partial \rho}{\partial y}, \frac{\partial v^2}{\partial y}, \frac{\partial M_A^2}{\partial y}, \frac{\partial B_z}{\partial y}, \frac{\partial B^2}{\partial y}, \frac{\partial \alpha}{\partial y}, \frac{\partial^2 A}{\partial y^2} \right] \quad (3)$$

$$\mathcal{Y} = \left[B_x \frac{dS_{\perp}}{dA}, B_x \frac{dS_{\parallel}}{dA}, B_x \frac{dH}{dA}, \frac{B_x}{\mu_0(1-\alpha)} \frac{dG^2}{dA}, B_x \frac{dC_z}{dA}, 0, 0, B_y \frac{\partial B_x}{\partial x}, \frac{Q}{1-\alpha} \right]. \quad (4)$$

The quantity Q in Equation (4) is $\text{RHS} - (\partial/\partial x)[(1-M_A^2)(1-\alpha)(\partial A/\partial x)]$, where RHS is the right-hand side quantity in (1) and the 9×9 matrix \mathbf{M} is referred to the overview paper by Sonnerup et al. (2006).

The GS type equations may be solved as a Cauchy problem using the observed plasma and magnetic field data and their derivatives, etc., as initial conditions. The reconstruction maps computed on the (x', y') plane with the invariant axis \hat{z}' are obtained by advancing the physical quantities away from the

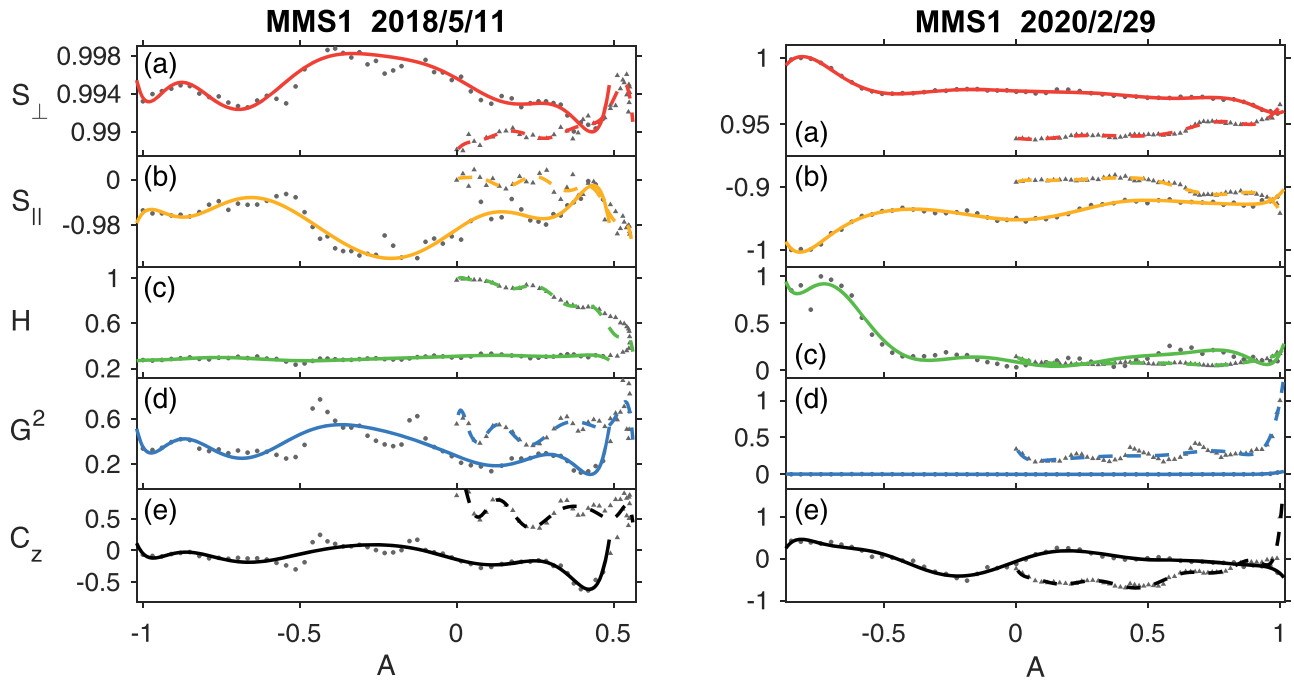


Figure 3. Polynomial fitting curves of the five field-aligned invariants. The dotted and triangle points are the observational data in the magnetosphere and magnetosheath, respectively, and the solid lines and dashed lines are the fitting curves, respectively.

spacecraft path (x' axis) (Hau & Sonnerup 1999). The DP GSR schemes have been benchmarked by the analytical solutions and applied to a THEMIS magnetopause crossing as well as three observed mirror wave events (Chen & Hau 2018; Hau et al. 2020). In the prior studies of magnetopause reconstruction the invariant axis is assumed to be on the plane perpendicular to the magnetopause normal and obtained by rotating the axis on the (M, L) plane with the optimal fittings between the five invariants and A (Hau & Sonnerup 1999; Chen & Hau 2018). In this study the choice of the invariant axis is based on rotating the axis around a sphere with the optimal fittings between the five invariants and A . It is found that the optimal invariant axes are mostly on the (M, L) plane and close to the M vector. Figure 3 shows the field-aligned invariants as functions of A for the observations and the two-branch fitting curves for the magnetosheath and magnetosphere separately (Hu & Sonnerup 2003). As shown in Table 1, the reconstruction coordinates are $\hat{x}' = (0.63, -0.135, 0.77)$, $\hat{y}' = (0.33, -0.85, -0.42)$, $\hat{z}' = (0.69, 0.48, -0.55)$ for MMS20180511, and $\hat{x}' = (0.02, 0.46, -0.89)$, $\hat{y}' = (-0.49, 0.78, 0.39)$, $\hat{z}' = (0.87, 0.43, 0.24)$ for MMS20200229, which are nearly the same for all four MMS spacecraft with various sets of polytropic values.

Figure 4 shows the reconstructed maps in the GSR coordinates (x', y', z') for MMS20180511 (Case A; left panels) and MMS20200229 (Case B; right panels) in which the white dotted points are the spacecraft path; the green arrows mark the observed magnetic field direction; the yellow arrows mark the measured residual flow velocity; and the magnetopause normal (white arrows) is also shown. Both events have a total of 100 data points and the reconstruction domains are about $2700 \text{ km} \times 2500 \text{ km}$ for Case A and $2800 \text{ km} \times 2100 \text{ km}$ for Case B. The background colors in panel (a) denote the magnetic field strength while the colors in panel (b) denote the ion number density. As indicated, the X lines are near the observational sites. The guide magnetic field (panel (e)) near the X lines is about -10 nT and -5 nT for Case A and

Case B, respectively, which are close to the values near the X lines obtained for other MMS events (Hasegawa et al. 2017).

For Case A (left panels) the features of density enhancements associated with decreased magnetic field are seen on both sides of the X line. While for Case B (right panels) the features of mirror waves such as the bottle-like magnetic field geometry are more pronounced on the magnetosheath's side of the reconnection. These results are consistent with the degrees of mirror instability shown in Figure 2. In particular, the features of mirror waves are more even for Case A with $m \sim 0$, while for Case B the mirror structures are more pronounced in the region of $m > 0$ (the magnetosheath's side) and less pronounced in the region of $m < 0$ (the magnetospheric side). The average sizes of the mirror waves are 370 km ($5.57\lambda_i/2.55r_{ci}$) in the magnetosheath and 170 km ($2.43\lambda_i/1.33r_{ci}$) in the magnetosphere for Case A. While the average sizes of the mirror waves are 298 km ($7.03\lambda_i/3.0r_{ci}$) in the magnetosheath and 243 km ($1.58\lambda_i/1.98r_{ci}$) in the magnetosphere for Case B. The pressure or temperature maps (panels (c) and (d)) indicate that the perpendicular components are greater than the parallel components for the entire reconstruction domains.

The reconstruction results shown in Figure 4 are obtained from the MMS1 spacecraft with $\gamma_{\perp} = 2$ and $\gamma_{\parallel} = 0.5$. The maps based on all four MMS spacecraft and four different sets of polytropic values including $(\gamma_{\perp} = 2, \gamma_{\parallel} = 3)$ and $(\gamma_{\perp} = 1, \gamma_{\parallel} = 1)$ in the energy closures show similar results. The mirror waves, however, are not revealed in the isotropic GSR with $d(p\rho^{-\gamma})/dt = 0$. The GSR results based on the MMS1 data can in principle predict the plasma and magnetic field at the MMS2, 3, and 4 spacecraft paths. The last three panels of Figure 1 show the three components of the magnetic field predicted by the GSR model using the MMS1 data (panel (a)) at the MMS2, 3, and 4 locations (panels (e), (f), and (g), respectively). The high agreements between the observed (colored curves) and predicted values (gray lines) provide a further validity check for the GSR model results. Note that the

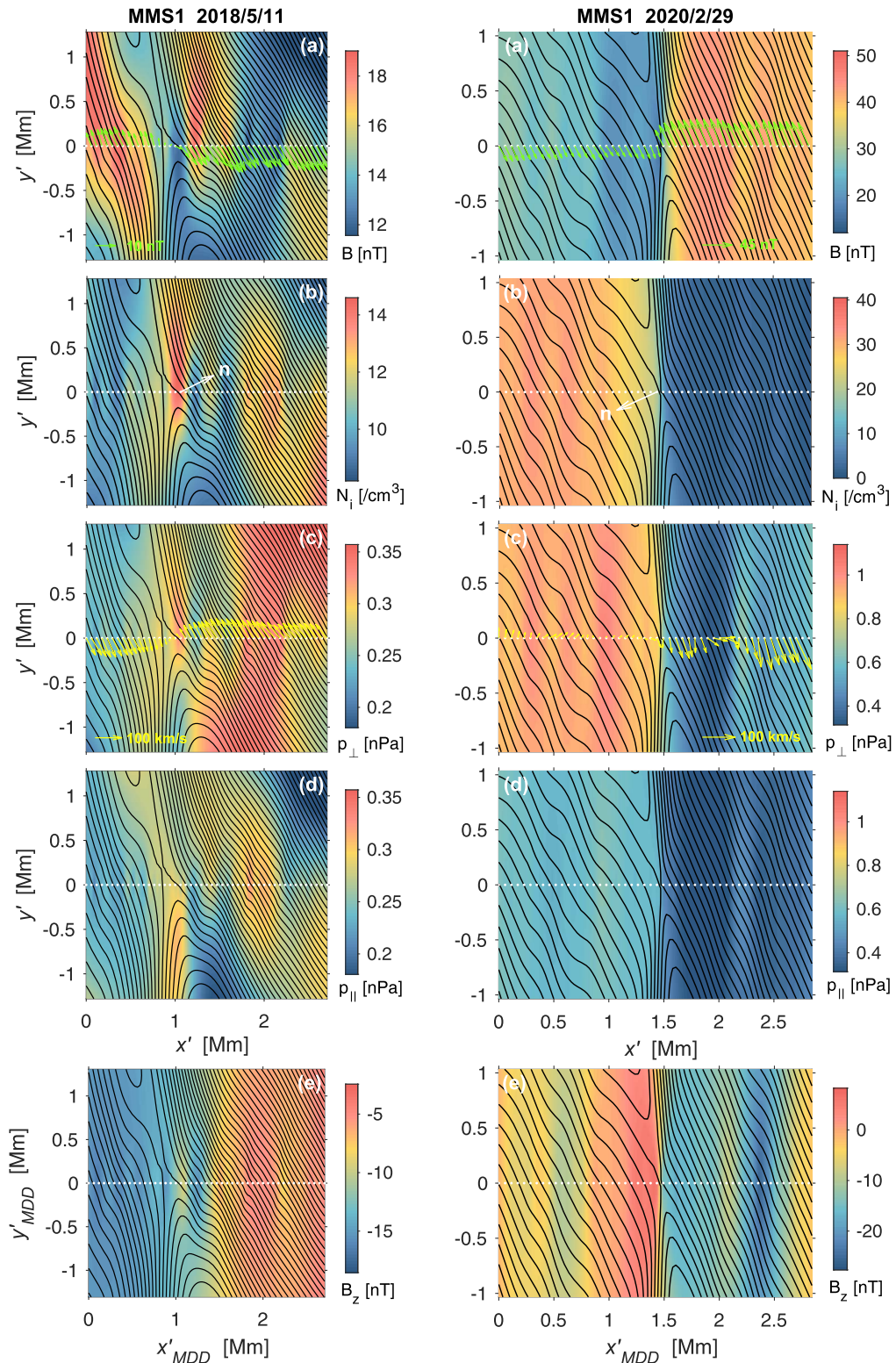


Figure 4. GSR results for MMS20180511 (left panels) and MMS20200229 (right panels) events. The (x', y') plane are the reconstruction plane perpendicular to the invariant axis \hat{z}' . The MVA-based invariant axis is used in panels (a)–(d) while the MDD-based invariant axis is used in panel (e). The white dots denote the spacecraft path; the white arrows mark the magnetopause normal; the green arrows denote the observed magnetic field direction; and the yellow arrows denote the measured ion velocity in the HT frame.

current density shown in panel (f) of Figure 2 are expressed in the GSR coordinates (x', y', z') with \hat{z}' being the invariant axis. As indicated, Case B (symmetric case) exhibits a strong current density component along the invariant axis (blue curve) while Case A (asymmetric case) has relatively weak current density.

Since the GS reconstructed magnetic field geometry may depend on the reconstruction coordinates, we have also adopted the minimum directional derivative (MDD) analysis for the determination of the invariant axis for 2D coherent structures (Shi et al. 2005). By using the magnetic field data from the four

MMS spacecraft, the calculated MDD-based invariant axis is $\hat{z}'_{\text{MDD}} = (0.8093, 0.4972, -0.3128)$ for Case A and $\hat{z}'_{\text{MDD}} = (0.9600, 0.1715, -0.2213)$ for Case B, which deviate from the MVA-based invariant axis shown in Table 1 by 15° and 31° , respectively. Indeed the angles between the MDD invariant axis and the magnetopause normal \hat{N} are close to 90° (101° for Case A and 97° for Case B), which are consistent with the invariant axis inferred from the MVA method. The MDD-based reconstruction field maps are shown in panel (e) of Figure 4 with the background colors being the magnetic field component along the invariant axis. As shown, the magnetic field geometry is nearly the same for two different choices of the invariant axis. The numerical experiments also show that the GS maps are similar for certain ranges of angles, say, 30° , with respect to the invariant axis shown in Table 1.

The two MMS events with a single X line are in contrast to the THEMIS event with few magnetic island analyzed by the same GS models (Chen & Hau 2018), which is likely due to the spacecraft paths relative to the current sheets as demonstrated by the benchmark experiments (Hau & Sonnerup 1999). In particular, the current sheets imbedded with multiple plasmoids separated by the X lines may appear to have a single X line geometry within the reconstruction domain provided that the spacecraft traverses across the current layers near the X line region, or, may exhibit few magnetic islands with relatively larger reconstruction domain for the magnetopause grazing events. Note that although the major goal of the MMS mission is to resolve the diffusion region (Burch et al. 2016), the captured magnetopause crossing events with the signatures of high magnetic shears are not necessarily close to the X line (Trattner et al. 2020). The events analyzed in this study are similar to the case identified by Hasegawa et al. (2017) for the study of the diffusion region in that the spacecraft paths are in the vicinity of MR sites (X lines) and the reconstruction maps shown in Figure 4 may simply be the small portions of larger elongated structures.



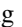
The features of mirror waves near the reconnection site have been predicted in the prior study of resistive tearing instability in Harris type current sheets with mirror type temperature anisotropy (see Figure 7 of Chiou & Hau 2002 and Figure 4 of Chiou & Hau 2003) which are, however, not apparent in the steady reconnection with a single X line (Hung et al. 2011). It is thus reasonable to conjecture that the field line geometry shown in Figure 4 is a small segment of the overall mixed tearing-mirror instability. It is interesting to note that Laitinen et al. (2010) have identified two Cluster magnetopause crossing events with fluctuated plasma flows accompanied by mirror waves in the magnetosheath and conjectured that the mirror events are associated with the patchy and bursty reconnection or the modulation of reconnection at a single X line. The sporadic mirror waves and plasma flows occurring on the timescale of one minute (for the crossing intervals of ~ 20 minutes) are not seen in the present MMS events, which span only $15 \sim 29$ s. Nevertheless their findings show several similarities with the mixed tearing-mirror instability, which for certain parameter regimes may become oscillatory and explosive (Chiou & Hau 2003). In particular, the X and O lines may take place alternatively and the outflow may sporadically reach the Alfvén speed with the oscillation periods of tens of Alfvén timescales (which are close to one minute for typical magnetopause parameters). More quantitative comparisons between the observations and theory are needed to reveal the various aspects of MR in anisotropic plasmas.

4. Summary

The two magnetopause crossing events observed by the MMS spacecraft exhibit common features of mirror waves adjacent to the X lines. The average plasma and magnetic field of both reconnection-mirror events may be well fitted by the symmetric (Case A) and asymmetric (Case B) current sheet equilibrium profiles with approximately constant total pressures. The magnetopause current density for the asymmetric case occurring in the dayside magnetopause is 10 times larger than the symmetric case occurring in the nightside magnetopause. The MR accompanied by the mirror waves appear to be the perturbations to the background Harris sheet equilibrium. These features are consistent with the plasma current sheets subject to the tearing mode instability or MR in anisotropic plasmas. In particular, the presence of mirror waves adjacent to the X line is in support of the theoretical prediction of mixed mirror-tearing instability in plasma current sheets (Chiou & Hau 2002, 2003). The average sizes of the mirror waves are about $6.3\lambda_i$ ($2.8r_{ci}$) and $2\lambda_i$ ($1.7r_{ci}$) in the magnetosheath and magnetosphere, respectively, smaller than the widths of the mirror waves typically observed in the outer magnetosheath (Hau et al. 2020). The kinetic mirror structures with ion gyroradius scale have been observed in the magnetotail currents (Sun et al. 2012) and are shown to exist near the magnetopause currents for the first time in the present study.

The MMS data can be accessed from MMS Science Data Center by following the link (<https://lasp.colorado.edu/mms/sdc/public/>). This research is supported by MOST109-2111-M-008-004 of Taiwan (R.O.C.) to National Central University.

ORCID iDs

L.-N. Hau  <https://orcid.org/0000-0003-0002-3037>
G.-W. Chen  <https://orcid.org/0000-0002-7964-3273>
C.-K. Chang  <https://orcid.org/0000-0001-9051-6307>

References

- Birn, J., & Hesse, M. 2001, *JGR*, **106**, 3737
Burch, J. L., Torbert, R. B., Phan, T. D., et al. 2016, *Sci*, **352**, aaf2939
Burlaga, L. F., Ness, N. F., & Acuna, M. H. 2007, *JGRA*, **112**, A07106
Chen, G.-W., & Hau, L.-N. 2018, *JGRA*, **123**, 7358
Chen, J., & Palmadesso, P. 1984, *PhFI*, **27**, 1198
Chiou, S.-W., & Hau, L.-N. 2002, *GeoRL*, **29**, 1815
Chiou, S.-W., & Hau, L.-N. 2003, *PhPI*, **10**, 3813
Chou, Y.-C., & Hau, L.-N. 2012, *JGRA*, **117**, A08232
Dunlop, M. W., Southwood, D. J., Glassmeier, K.-H., & Neubauer, F. M. 1988, *AdSpR*, **8**, 273
Ferrière, K. M., & André, N. 2002, *JGRA*, **107**, 1349
Furth, H. P., Killeen, J., & Rosenbluth, M. N. 1963, *PhFI*, **6**, 459
Gershman, D. J., Dorelli, J. C., Viñas, A. F., Avakov, L. A., et al. 2016, *GeoRL*, **43**, 4112
Graham, D. B., Khotyaintsev, Yu. V., Vaivads, A., et al. 2014, *PhRvL*, **112**, 215004
Guo, F., Liu, Y.-H., Daughton, W., & Li, H. 2015, *ApJ*, **806**, 167
Haaland, S., Paschmann, G., Øieroset, M., Phan, T., et al. 2020, *JGRA*, **125**, e27623
Harris, E. G. 1962, *NCim*, **23**, 115
Hasegawa, A. 1969, *PhFI*, **12**, 2642
Hasegawa, H., Sonnerup, B. U. Ö., Denton, R. E., et al. 2017, *GeoRL*, **44**, 4566
Hasegawa, H., Sonnerup, B. U. Ö., Dunlop, M. W., et al. 2004, *AnGeo*, **22**, 1251
Hau, L.-N., & Sonnerup, B. U. Ö. 1993, *GeoRL*, **20**, 1763
Hau, L.-N., & Sonnerup, B. U. Ö. 1999, *JGR*, **104**, 6899
Hau, L.-N., Chang, C.-K., & Chen, G.-W. 2020, *ApJ*, **900**, 97
Hau, L.-N., & Chiou, S. W. 2001, *JGR*, **106**, 8371
Horbury, T. S., & Lucek, E. A. 2009, *JGRA*, **114**, A05217

- Hu, Q., & Sonnerup, B. U. Ö. 2003, *JGRA*, **108**, 1011
- Hu, Q., Smith, C. W., Ness, N. F., & Skoug, R. M. 2003, *GeoRL*, **30**, 1385
- Hung, C.-C., Hau, L.-N., & Hoshino, M. 2011, *GeoRL*, **38**, L18106
- Joy, S. P., Kivelson, M. G., Walker, R. J., et al. 2006, *JGRA*, **111**, A12212
- Laitinen, T. V., Khotyaintsev, Y. V., André, M., Vaivads, A., et al. 2010, *AnGeo*, **28**, 1053
- Landi, S., Zanna, L. D., Papini, E., Pucci, F., et al. 2015, *ApJ*, **806**, 131
- Liu, H., Zong, Q.-G., Zhang, H., Xiao, C. J., et al. 2019, *NatCo*, **10**, 1040
- Paschmann, G., Sonnerup, B. U. Ö., Papamastorakis, I., et al. 1979, *Natur*, **282**, 243
- Petschek, H. E. 1964, in AAS/NASA Symp. Physics of Solar Flares: Proc. Symp., ed. W. N. Hess (Science and Technical Information Division, Washington: NASA), 425
- Pollock, C., Moore, T., Jacques, A., et al. 2016, *SSRv*, **199**, 331
- Russell, C. T., Anderson, B. J., Baumjohann, W., et al. 2016, *SSRv*, **199**, 189
- Shi, Q. Q., Shen, C., Pu, Z. Y., Dunlop, M. W., et al. 2005, *GeoRL*, **32**, L12105
- Shi, Y., Lee, L. C., & Fu, Z. F. 1987, *JGR*, **92**, 12171
- Sonnerup, B. U. Ö., Hasegawa, H., Teh, W.-L., & Hau, L.-N. 2006, *JGRA*, **111**, A09204
- Sonnerup, B. U. Ö., Hau, L.-N., & Walthour, D. W. 1992, *JGR*, **97**, 12015
- Sonnerup, B. U. Ö., Papamastorakis, I., Paschmann, G., & Lühr, H. 1987, *JGR*, **92**, 12137
- Sun, W. J., Shi, Q. Q., Fu, S. Y., et al. 2012, *AnGeo*, **30**, 583
- Teh, W.-L. 2019, *JGRA*, **124**, 1164
- Tian, A., Xiao, K., Degeling, A. W., et al. 2020, *ApJ*, **889**, 35
- Trattner, K. J., Burch, J. L., Fuselier, S. A., Petrinec, S. M., & Vines, S. K. 2020, *JGRA*, **125**, e27617
- Tsurutani, B. T., Lakhina, G. S., Verkhoglyadova, O. P., et al. 2011, *JGRA*, **116**, A02103
- Vaivads, A., Khotyaintsev, Y., André, M., et al. 2004, *PhRvL*, **93**, 105001
- Yao, S. T., Shi, Q. Q., Yao, Z. H., et al. 2019, *GeoRL*, **46**, 523
- Zhong, Z. H., Zhou, M., Tang, R. X., Deng, X. H., et al. 2020, *ApJL*, **892**, L5